Information transmission by Marangoni-driven relaxation oscillations at droplets

Mokbel, M.; Schwarzenberger, K.; Aland, S.; Eckert, K.;

Information transmission by Marangoni-driven relaxation oscillations at droplets[†]

Marcel Mokbel,[a‡] Karin Schwarzenberger,[*b‡] Sebastian Aland,[a] and Kerstin Eckert[b,c]

Marangoni-driven relaxation oscillations can be observed in many systems where concentration gradients of surface-active substances exist. In the present paper, we describe the experimentally observed coupling between relaxation oscillations at neighboring droplets in a concentration gradient. By a numerical parameter study, we evaluate the oscillation characteristics depending on relevant material parameters and the pairwise droplet distance. Based on these findings, we demonstrate that hydrodynamic interaction in multidroplet configurations can lead to a synchronization of the oscillations over the whole ensemble. This effect has the potential to be used as a novel approach for information transmission in microfluidic applications.

1 Introduction

Complex sequences of microfluidic processes can be condensed on extremely small platforms as realized in lab-on-a-chip devices. This generates the need for alternative approaches in signal transmission like microfluidic networks[1] or molecular communication[2] for an enhanced process control and flexibility. Marangoni convection offers a promising tool to convey information in such devices. This flow is triggered by gradients in interfacial tension due to concentration variations of a surface-active solute (soluto-capillary case) or temperature variations (thermocapillary case). The resulting high velocity magnitudes, which operate on small scales, are particularly suitable for the limited space in microfluidic channels. These characteristics are utilized in recent works by specifically introducing fluidic interfaces in capillary channels to create a Marangoni-based micromixer[3–5]. Furthermore, the Marangoni effect is an elegant method for a controlled droplet actuation[6–8] even capable of substituting the geometrical microfluidic structure via an externally imposed temperature distribution on a planar liquid film[9]. Marangoni convection also allows the small-scale patterning of films to manufacture functional surfaces[10,11] or the structured deposition of nanoparticles from evaporating droplets[12,13]. These developments are supported by continuing basic research on Marangoni pattern formation which provides a detailed understanding of the complex spatio-temporal evolution of the flow[14–19].

Besides the pattern resulting from hydrodynamic instability over the whole interface, interaction of discrete neighboring sources of Marangoni convection can likewise lead to convective structures. In[20], multiple droplets of partially miscible fluid are dissolving in a surrounding liquid with an imposed vertical temperature gradient. They show diverse convective modes depending on the number of droplets and the presence of surface Marangoni effects. A completely different approach to create surface tension gradients is pursued in[21]. This theoretical study considers an interface with photoresponsive surfactants which change their surface activity due to illumination. Coupling the intensity of discrete light spots to the local advection velocity by feedback control results in the formation of complex patterns including periodically switching states. The Marangoni effect is able to propel or deform emulsion droplets immersed in the surrounding phase[22,23] or floating on the liquid surface[24,25]. Ensemble interactions between multiple droplets give rise to various collective phenomena like dynamic ordering, clustering and synchronized deformation.

Such self-propelled droplets are frequently used to model biological systems like micro-organisms[26,27]. In this way, the complex interplay of hydrodynamics, external gradient fields and biological signals on the group dynamics can be broken down to unravel the main influence parameters. The need for these controllable model systems to understand different swarming mechanisms is reflected in the diversity of biological systems. Indeed, spatio-temporal pattern can form in a dense population of self-propelling cells by purely hydrodynamic interactions without the exchange of chemical signals between the cells[28]. A second example is the spreading of bacteria on nutrient-rich subphases

[a] Faculty of Informatics/Mathematics, HTW Dresden, 01069 Dresden, Germany
[b] Institute of Fluid Dynamics, Helmholtz-Zentrum Dresden-Rossendorf, 01328 Dresden, Germany
[c] Institute of Process Engineering and Environmental Technology, TU Dresden, 01062 Dresden, Germany
[*] E-mail: k.schwarzenberger@hzdr.de
[†] Electronic Supplementary Information (ESI) available: See DOI: 10.1039/cXsm00000x/
[‡] These authors contributed equally to this work.

which is controlled by different physico-chemical mechanisms. An efficient strategy for the spreading is the production of strong bio-surfactants[29]. The collective secretion induces a Marangoni flow in the bacterial biofilm, which rapidly expands the colony in fingering patterns. The coupling of discrete elements leading to spatio-temporal patterns of the whole ensemble can also be found in biological communication schemes[30,31]. In such systems, it is often advantageous to exploit the signal dynamics rather than steady-state information[32,33].

In our work, the dynamic signal is created by Marangoni-driven relaxation oscillations at single droplets placed in a concentration gradient of surface-active solute. Here, a short active phase of Marangoni convection periodically alternates with a long relaxation phase. In the active phase, the Marangoni convection consumes the driving concentration gradient. In the relaxation phase, the gradient is restored by diffusion and buoyancy-driven convection. This repeated coupling of consuming and regenerating processes which take place on different timescales is summarized by the term "relaxation oscillations". Relaxation oscillations are not limited to this specific configuration but are known from many dynamic systems like density oscillators[34], human heartbeat or electronic relaxation oscillators[35]. Marangoni-driven relaxation oscillations at droplets or bubbles were observed in various fluid combinations where concentration gradients of surface-active substances exist[36–40]. A similar periodicity is obtained by the spreading of a strong surfactant from a droplet located under a plane surface or an interface[41,42]. Here, a single convection cell decays and rekindles due to the combined action of adsorption-desorption kinetics and geometric confinement. Generally, the characteristic times of such Marangoni-driven relaxation oscillations depend on the material parameters of the fluids and solutes[37,38,43,44].

This potential to control the oscillation dynamics together with the rather simple set-up of droplets placed in a concentration gradient makes the Marangoni-driven relaxation oscillations an excellent candidate for the study of ensemble convective interaction. In our work, we show the strong feedback between relaxation oscillations at neighboring droplets. The droplets themselves are static in position, which reduces the complexity of our system compared to mobile droplets. By such coupled oscillations, it is possible to use the droplets as a novel medium to propagate a signal along a distance manifold exceeding the diameter of a single droplet. The small length scale of the observed phenomena opens the possibility to utilize this effect for information transmission in microfluidic applications.

The first part of our study (Sec. 3.1) provides the basis for controlled oscillation dynamics by considering a single droplet. Therefore, we characterize the structure of the flow and the influence of the governing parameters on the relaxation oscillations. The second part (Sec. 3.2) is devoted to interacting droplets. We present experimental observations of coupled oscillations at neighboring droplets. By numerical simulations, we determine the optimal distance between two droplets for synchronized oscillations. Finally, we study two different multidroplet configurations where information, i.e. oscillation with a certain frequency and amplitude, is conveyed along a defined path.

2 Methods

2.1 Experimental system

Our chemical system consists of three common substances: liquid paraffin, water and 2-propanol (isopropanol). All chemicals are used as purchased. Water and 2-propanol are of HPLC grade, and liquid paraffin is of pharmaceutical quality (Ph.Eur., DAB). The relevant material parameters of the system are summarized in Table 1. They are taken from the literature or estimated by suitable relationships as described in[40]. Liquid paraffin containing 5 vol-% 2-propanol and water are filled in the narrow gap of a Hele-Shaw cell (gap width 1 mm) forming a two-layer system with an upper organic phase (2) and a lower aqueous phase (1). The width and height of each layer amount to approx. 20 mm and 35 mm, respectively. The exact geometry of the Hele-Shaw cell as well as the filling procedure are explained in detail in[40,45]. During the filling, small droplets of the oil phase remain in the aqueous phase at the glass wall of the Hele-Shaw cell. As shown in Fig. 2(a), the droplets are located at different distances from the overlying interface of the two liquid layers. The diameter of the droplets is typically 0.2 – 0.5 mm, corresponding to a volume of a few nanoliters.

The two-layer system serves to form a concentration gradient in the aqueous phase surrounding the droplets. Due to the hydrophilic nature of the short-chain alcohol 2-propanol, partition is largely in favor of the aqueous phase. This leads to an intense mass transfer from the organic to the aqueous layer and, accordingly, to a concentration gradient of 2-propanol evolving in the aqueous phase. This concentration gradient has two consequences, which are important for our study: An increasing 2-propanol concentration lowers both the density of the aqueous phase surrounding the droplets and the interfacial tension at the droplet surface. For the dependence of the aqueous solution density $\rho^{(1)}$ and the interfacial tension σ on 2-propanol concentration c, a linear relationship based on a solutal expansion coefficient β_c and an interfacial tension coefficient α_c is assumed[40]. Hence, a stable density stratification establishes in the fluid surrounding the droplets and gradients of interfacial tension build up. This leads to a periodic Marangoni convection interacting with buoyancy-driven convection and diffusion. In[40] we showed that this phenomenon can be observed at various droplets and also bubbles in our chemical system. A mechanism was proposed for the temporal evolution of the convection describing it as relaxation oscillations.

Now we largely extend this knowledge by evaluating the influence of the system parameters, which control the characteristics of the relaxation oscillations. Therefore, we make use of the specific conditions given by the mass transfer of 2-propanol over the interface of the two-layer system and of a defined parametric study in numerical simulations described in the following section.

2.2 Numerical simulations

The mathematical model underlying our simulations is presented in the previous work of Schwarzenberger et al.[40]. Hence, we only provide the main aspects here and refer to the previous work for detailed information. We use a diffuse interface model to simulate

Description	Symbol	Unit	Value	Ref.
Molar mass water	$M^{(1)}$	kg/mol	$18.02 \cdot 10^{-3}$	[46]
Molar mass paraffin oil (eicosane)	$M^{(2)}$	kg/mol	$282.55 \cdot 10^{-3}$	[46]
Molar mass 2-propanol	M_p	kg/mol	$60.10 \cdot 10^{-3}$	[46]
Mass density water	$\rho_{ref}^{(1)}$	kg/m^3	998	[46]
Mass density paraffin oil	$\rho_{ref}^{(2)}$	kg/m^3	850	[47]
Mass density 2-propanol	ρ_p	kg/m^3	781	[46]
Dynamic viscosity water	$\eta^{(1)}$	$Pa \cdot s$	$1.00 \cdot 10^{-3}$	[46]
Dynamic viscosity paraffin oil	$\eta^{(2)} = v^{(2)} \rho_{ref}^{(2)}$	$Pa \cdot s$	$28.9 \cdot 10^{-3}$	
Kinematic viscosity paraffin oil	$v^{(2)}$	m^2/s	$34 \cdot 10^{-6}$	[47]
Oil/water partition coefficient of 2-propanol	H	$(mol/l)/(mol/l)$	0.16	[48]
Diffusivity 2-propanol in water	$D^{(1)}$	m^2/s	$1.08 \cdot 10^{-9}$	[49]
Diffusivity 2-propanol in paraffin oil	$D^{(2)}$	m^2/s	$9 \cdot 10^{-11}$	[50]
Oil/water interfacial tension	σ_{ref}	N/m	$50.1 \cdot 10^{-3}$	[48]
Interfacial tension coefficient	α_c	l/mol	-2.71	[48]
Solutal expansion coefficient 2-propanol in water	β_c	l/mol	-0.0167	
Initial conc. for 5 vol% 2-propanol in paraffin oil	c_0	mol/l	0.649	
Gravitational acceleration	g	m/s^2	9.81	

Table 1 Properties of the system liquid paraffin/water with interfacial mass transfer of 2-propanol; Phase 1 is the aqueous phase marked with upper index [1] and phase 2 the organic phase marked with [2]

the two-phase flow problem with a surface-active solute[51]. Motivated by the experimental set-up, we assume a 2D Hele-Shaw situation[52] with a parabolic velocity profile across the gap of the Hele-Shaw cell. The droplet therefore is modeled as a cylindrical fluid domain between the plates. The mass transport is expressed by an advection-diffusion equation and the momentum transport by the incompressible Navier–Stokes equations coupled with the Marangoni shear stress balance at the interface. We validated numerically[40] that the inertia term in the Navier-Stokes equations can be omitted in the considered parameter regime. As initial condition, we suppose that the fluid is at rest ($\mathbf{v} = 0$). The aqueous phase surrounding the droplets is modeled by a rectangular fluid domain of size $L_x \times L_y$ with an initially constant vertical concentration gradient of 2-propanol ($c(y) = k_c y$). That means, the non-steady state in the experiment with an evolving concentration profile in the aqueous phase is approximated by a steady-state concentration field with a constant concentration gradient. Since the initial concentration distribution is predefined in the simulations, the liquid paraffin layer (overlying the aqueous phase in the experiments) is disregarded. Furthermore, the solute concentration in the droplets is neglected due to the low partition coefficient. We apply the Boussinesq approximation and Henry's model so that the aqueous solution density $\rho^{(1)}$ and interfacial tension σ depend linearly on the concentration c of 2-propanol:

$$\rho^{(1)} = \rho_{ref}^{(1)} + \rho_{ref}^{(1)} \beta_c c, \tag{1}$$

$$\sigma = \sigma_{ref} + \sigma_{ref} \alpha_c c, \tag{2}$$

with the solutal expansion coefficient β_c, the reference density of water $\rho_{ref}^{(1)}$, the reference interfacial tension of the oil/water system σ_{ref}, and the interfacial tension coefficient of 2-propanol α_c.

At the lateral boundaries, we assume a no flux condition ($\mathbf{n} \cdot \nabla c = 0$). At the lower boundary, the concentration is set to zero ($c(0) = 0$). At the upper boundary, the concentration is held fixed to the value $c(L_y) = k_c L_y$. For the velocity, a no-slip condition ($\mathbf{v} = 0$) is imposed on all boundaries. A domain size of $L_x \times L_y = 8 \text{ mm} \times 8 \text{ mm}$ is used in the single droplet simulations. Fig. 1 shows that the oscillation period, which characterizes the dynamics of the convection, is approximately invariant on domain size for domains larger than this. For the multi-droplet configuration, the domain size is $L_x \times L_y = 8 \text{ mm} \times 10 \text{ mm}$ to ensure approximately the same minimum distance of the droplets from the domain boundaries. The grid resolution is adapted to capture the fine structures arising during Marangoni convection. The mesh size (longest side of triangles) amounted to $3.906 \cdot 10^{-5}$ m at the interface and $1.5625 \cdot 10^{-4}$ m in the bulk phase.
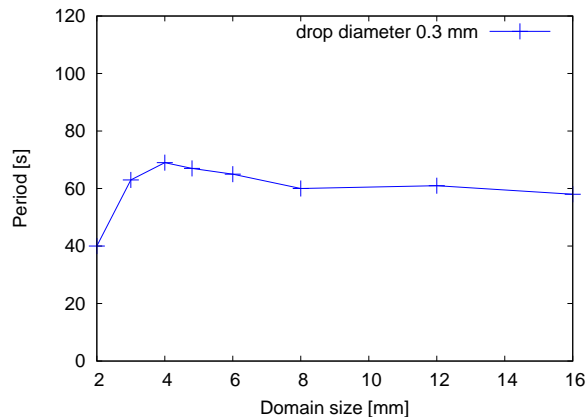

Fig. 1 Oscillation period over domain size for reference simulation parameters.

For the single-droplet reference simulation, we chose input parameters corresponding to our experimental conditions[40]. The droplet size was set to $2r = 0.3$ mm and the initial concentration gradient to $dc/dy = k_c := 25.4$ mol/(l·m). The remaining material parameters are summarized in Table 1. Based on these settings, we varied the solutal expansion coefficient β_c, the interfacial tension coefficient α_c, the solute diffusivity in the aqueous phase $D^{(1)}$

and the droplet radius r as shown in Sec. 3.1.2. Furthermore, we studied the influence of the droplet distance for two interacting droplets (cf. Sec. 3.2.2).

3 Results

3.1 Relaxation oscillations at single droplets

3.1.1 Dependence of oscillation frequency in experiment

In this section, we describe experimentally observed relaxation oscillations at liquid paraffin droplets in the aqueous phase which motivated our subsequent numerical study. The snapshot in Fig. 2(a) is recorded via a shadowgraph optics. This technique is sensitive towards the second derivative (Laplacian) of the refractive index field[53] and therefore can visualize structures in the concentration field if the solute changes the refractive index of the fluid. In our experiment, 2-propanol diffuses into the aqueous phase due to the mass transfer from the overlying organic phase (liquid paraffin with 5 vol-% 2-propanol). The interface separating both phases appears as a solid black line in Fig. 2(a). It is slightly deformed due to the filling of the liquids in the Hele-Shaw cell. At the right margin, a pinning edge is visible which belongs to the design of the experimental container[45]. The droplets in the aqueous phase, numbered 1–4 in Fig. 2, appear as black circular dots due to their high interfacial curvature shadowing the transmitted light in the optical path. The concentration gradient resulting from the 2-propanol mass transfer triggers relaxation oscillations of Marangoni convection at the droplets.

This mechanism forms the key stone of our study and can be explained as follows[40]. The droplets are subjected to high solute concentration at the upper side, implying both low interfacial tension σ and density $\rho^{(1)}$, and low concentration at the bottom, i.e. both higher σ and $\rho^{(1)}$. Therefore, Marangoni convection at the droplet surface is directed downwards, entraining lighter fluid rich in solute to lower regions of higher density. The initially stably stratified aqueous phase is stirred, and the additional buoyancy accelerates the rise of the lighter fluid at some distance from the droplet surface. As a result, an intense mixing of the fluid takes place which rapidly exhausts the vertical concentration gradient in the vicinity of the droplet and leads to the breakdown of Marangoni convection.

The mixed fluid is visible as a double vortex with high black-and-white contrast around each droplet in Fig. 2(a), particularly pronounced at droplet 1 and 2. This feature is used in the graph in Fig. 2(b) to display the temporal evolution of convection. We evaluate the standard deviation $s = \sqrt{\frac{1}{n-1}\sum_{i=1}^{n}(G_i - \bar{G})^2}$ of the gray values G_i in a rectangular image section of approx. 500 pixels in the surrounding region of the respective droplet, where $\bar{G} = \frac{1}{n}\sum_{i=1}^{n}G_i$ is the mean gray value of the n pixels. The image section is chosen such as to avoid interference of convection from the other droplets, e.g. a region at the lower right side was analyzed for droplet 4. In the state of active Marangoni convection, the contrast and therefore the standard deviation of gray values is high. This corresponds to a rise of the curves in Fig. 2(b). In the subsequent relaxation phase, the initial vertical concentration gradient is slowly restored by both the buoyancy-driven

convection, which carries the mixed fluid upwards, and diffusion. Thereby, the mixed region surrounding the droplets fades and the standard deviation in Fig. 2(b) decreases. When the vertical concentration gradient of 2-propanol is rebuilt, the next cycle of Marangoni convection starts. This repeated process leads to the relaxation oscillations in the curves of Fig. 2(b). The evolution of convection at droplet 4 is not shown in this graph, because it is strongly influenced by the overlying droplet 3, as will be discussed later (see Sec. 3.2.1).

Fig. 2(b) indicates that the oscillation frequency depends on the droplet position, i.e. on the surrounding concentration gradient. The acting concentration gradient however is determined not only by the position of the particular droplet, but also by the length of time. This is visible in Fig. 3(a), where the oscillation frequency is plotted over time for droplet 1–3. The starting time $t = 0$ is defined as the end of the filling procedure. In this graph, the frequency $f = 1/T_p$ is defined as the inverse period T_p, i.e. the inverse time span between two neighboring peaks in the standard deviation curves. Depending on the droplet position, characteristic progressions of the oscillation frequency are obtained. As the concentration gradient advances into the aqueous bulk phase, the convection first sets in at droplet 1, followed by droplet 2 and 3. The curve for droplet 1 (red squares) rapidly rises to a maximum of 0.1 Hz and drops again afterwards. The discrete frequency values result from the framerate of the shadowgraph records which is set to 2 Hz. Droplet 2 (green circles) likewise shows an initial increase of oscillation frequency followed by a decrease, but its frequency maximum is lower and shifted to later times. For droplet 3 (blue triangles), only a moderate rise can be observed without reaching a clear maximum in the duration of the experiment.

Since it is the concentration gradient along the droplet surface which causes the relaxation oscillations, we estimate its dependence on time and distance from the interface of the two-layer system to interpret the frequency values. The time-dependent concentration profile $c(y,t)$ for the diffusion process in the accepting aqueous phase resulting from an initial concentration c_0 in the donating organic phase takes following well-known form[54]:

$$c_{diff}(y,t) = \frac{H^{-1}c_0}{1 + H^{-1}\sqrt{D^{(1)}/D^{(2)}}}\text{erfc}\frac{|y|}{2\sqrt{D^{(1)}t}}. \tag{3}$$

We remark that the interface is located at $y = 0$ and that $y < 0$ holds in the lower aqueous phase according to the notation of Eq. (3). Fig. 3(b) depicts the concentration gradient $(\text{d}c/\text{d}y)_{diff}$ derived from Eq. (3) as a function of time for defined distances to the interface. These distances correspond to droplet 1 (1 mm, red curve with "+"-symbols), droplet 2 (2 mm, green curve with crosses) and droplet 3 (3.6 mm, blue curve with asterisks). The curves resemble the temporal evolution of oscillation frequency in Fig. 3(a). This comparison suggests that the acting concentration gradient dominates the characteristics of the relaxation oscillations and that slight variations of other parameters like the droplet size are of minor influence. For droplets which are subjected to a high concentration gradient (like droplet 1), large velocities are obtained both for the Marangoni- and the buoyancy-
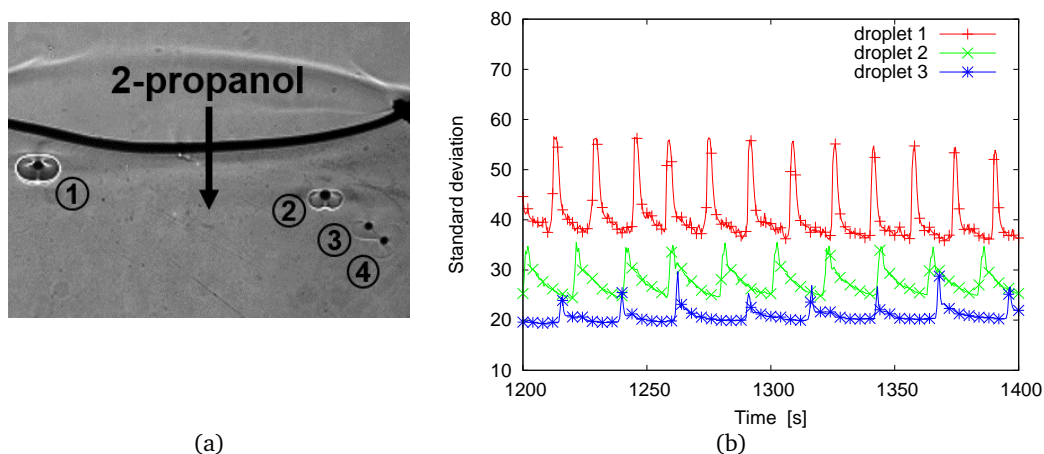
(a)

(b)

Fig. 2 Relaxation oscillations for different droplets in the aqueous phase: (a) Shadowgraph image of the active phase of Marangoni convection at different droplets; the width of the shown window is 15 mm. The black arrow indicates the mass transfer of 2-propanol over the interface of the two-layer system. The vector of gravitational acceleration is parallel to the black arrow. (b) Temporal evolution of standard deviation of gray value distribution around droplets 1–3.
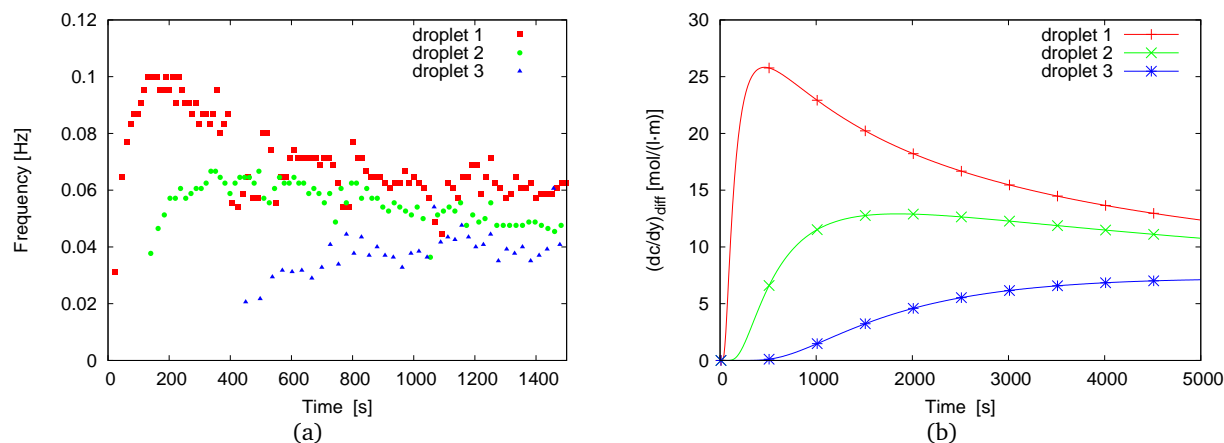

(a)

(b)

Fig. 3 Temporal evolution of (a) oscillation frequency for droplet 1–3 in comparison with (b) the vertical concentration gradient $(dc/dy)_{diff}$ for purely diffusive mass transfer of 2-propanol from the organic into the aqueous layer.

driven convection at the droplet. Thus, the temporal evolution of both the active and the relaxation phase is accelerated leading to a higher oscillation frequency.

Indeed, Fig. 3 is restricted to a *qualitative* comparison between oscillation frequency and driving concentration gradient. This is visible in the larger time scale of the abscissa for the diffusive concentration gradient $(dc/dy)_{diff}$. The difference is attributed to the convective mass transfer of 2-propanol enhancing the propagation of the solute front into the aqueous phase. Marangoni convection is not only initiated at the droplets but also at the interface of the two-layer system itself, visible as a light-gray arc in the upper part of Fig. 2(a). Although these aspects are neglected for the rough estimation based on purely diffusive mass transfer, Fig. 3 underlines the role of the concentration gradient as driving force for the relaxation oscillations.

3.1.2 Numerical characterization of relaxation oscillations

3.1.2.1 Velocity and concentration distribution. The numerical simulations of a droplet placed in an initially constant vertical concentration gradient provide a deeper understanding of the above-described experimental observations. Fig. 4 shows the 2D concentration and velocity distribution around the droplet for the state of active Marangoni convection and directly after its breakdown (corresponding to state 3 and 5 as defined below). For the sake of visual clarity, velocity vectors of equal length are plotted to illustrate the structure of the flow. The active phase in Fig. 4(a) is characterized by the Marangoni-driven downstream at the droplet surface and the buoyancy-driven rise in the surrounding fluid leading to the double vortex already observed in the experiments. Because of the decline of interfacial convection, the structure of the flow essentially changes from active to relaxation phase. Fig. 4(b) reveals that the main flow direction in the surrounding of the droplet is inverted and the buoyancy-driven rise becomes dominant.
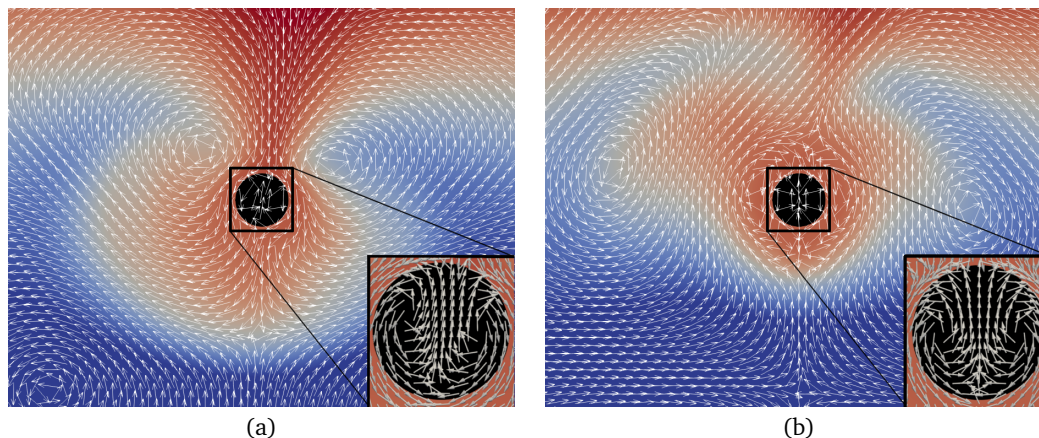
Fig. 4 Velocity (vectors of equal length) and concentration field (color coding) in the single-droplet reference simulation with close-up views of the velocity profile inside the droplets. (a) Peak of interfacial velocity in state 3, (b) lowest interfacial velocity in state 5. The droplet diameter (0.3 mm) serves as a scale bar.

The temporal evolution is further detailed in Fig. 5. Fig. 5(a) displays the mean interface velocity and the mean interface concentration during a full oscillation period. Five characteristic states are marked at the velocity curve (red line), indicating the corresponding times for the velocity profiles in Fig. 5(b). These profiles depict the distribution of the vertical velocity component v_y over a horizontal line beginning at the center of the droplet, crossing the interface and extending 1.5 mm towards the right boundary of the numerical domain. The five characteristic states are defined as follows:

1. relaxation phase: point of time well within the long phase of low interfacial convection

2. velocity rise: maximum positive slope of interfacial velocity curve

3. velocity peak: maximum of interfacial velocity curve

4. velocity decrease: maximum negative slope of interfacial velocity curve

5. lowest velocity: minimum of interfacial velocity curve

The quiescent relaxation phase (state 1) is chosen as a starting point of the oscillation period shown in Fig. 5(a). As visible in Fig. 5(b), a slight Marangoni flow directed downwards at the interface still exists in this state, but the flow remains at a low velocity magnitude for quite a long time. In state 2, the concentration gradient in the surrounding of the droplet is sufficiently restored so that the Marangoni flow is rapidly amplified to reach its peak in state 3. The 2D concentration and velocity distribution in Fig. 4(a) demonstrates the reason for this amplification. Due to the downflow at the droplet surface, solute-rich fluid is sucked to the top region of the droplet thereby enhancing the interfacial tension difference between the top and the bottom of the droplet. As a result of this intense advection of solute, the interface concentration increases in Fig. 5(a). The velocity profiles in Fig. 5(b) illustrate the growing interfacial downflow in state 2 and 3. Furthermore, two recirculation zones with positive vertical velocities establish by continuity. One is located in the droplet center, i.e. towards a distance of zero in Fig. 5(b). The second upflow, which

is supported by the rise of the lighter solute-rich fluid due to buoyancy convection, forms in the outer regions (distance > 0.5 mm). In consequence of this recirculation, the mixing zone builds up, visible as a region of homogeneous color in the concentration distribution of Fig. 4, finally causing the breakdown of interfacial convection in state 4. Note that a small secondary velocity peak is visible in Fig. 5(a) which is connected to the upstream of solute-rich fluid right at the termination of the active phase. Shortly after, the state 5 of lowest interfacial convection is reached. Even if the flow structure within the droplet remains similar to state 3 (see detail of Fig. 4), the corresponding velocity magnitudes in Fig. 5(b) are close to zero in state 5. Without the opposing Marangoni convection, the buoyancy-driven upflow shifts close to the droplet surface. The restoring processes of buoyancy-driven convection and diffusion cause the decrease of interfacial concentration in Fig. 5(a) whereby the oscillation cycle closes.

3.1.2.2 Variation of important system parameters. As stated in the previous sections, the interaction of three physical mechanisms causes the occurrence of the relaxation oscillations: Marangoni convection, buoyancy convection and diffusion. In terms of the material parameters in Table 1, these mechanisms are represented by:

- α: interfacial tension coefficient
- β: solutal expansion coefficient
- $D^{(1)}$: diffusivity of surface-active solute in the aqueous phase

To estimate their influence on the oscillation dynamics, each of these main parameters is varied separately by a factor of 0.3 to 10 (compared to the reference simulation) in following steps: 0.3, 1, 3, 10, while all other parameters are kept constant. Furthermore, to check the robustness of the observed phenomena on the droplet size, two more simulations are performed with doubled and halved droplet radius r. Based on the definition of relaxation oscillations as repeated coupling of a short active and a long relaxation phase, we define two characteristic oscillation times from the temporal evolution of surfactant concentration (blue crosses) in Fig. 5(a). The active phase is represented by the time span
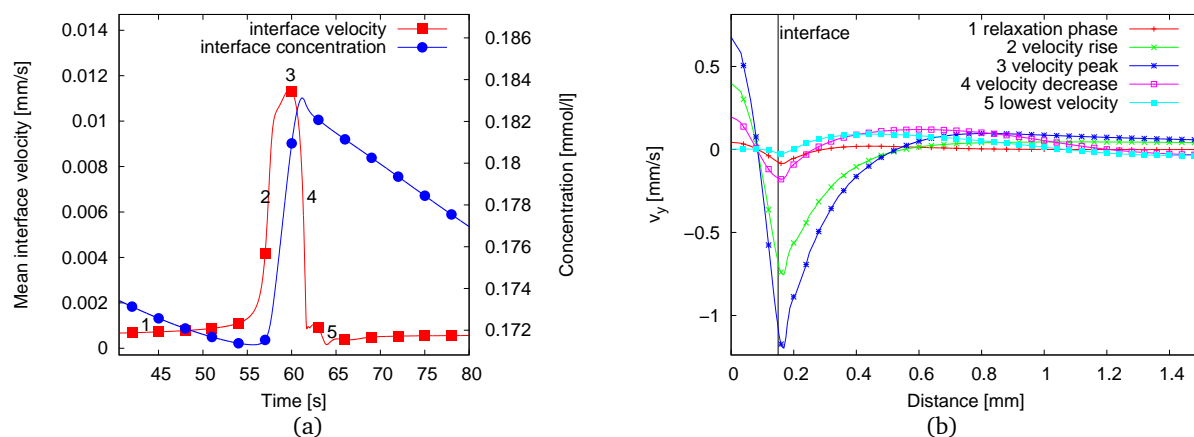
Fig. 5 One oscillation period in the single-droplet reference simulation. Numbers refer to five characteristic states of the temporal evolution. (a) Mean interface velocity (left axis, plus symbols) and concentration development (right axis, crosses). (b) Profiles of vertical velocity v_y over a horizontal line starting at the droplet center. The black vertical line marks the position of the interface.

of rising surfactant concentration, denoted t_{rise}, and the relaxation phase by the time span of decreasing surfactant concentration t_{relax}. In Fig. 6, these characteristic oscillation times are plotted over the relative parameter values α/α_{ref}, β/β_{ref}, $D^{(1)}/D^{(1)}_{ref}$. Since Marangoni convection dominates the active phase of the relaxation oscillations, t_{rise} is used to show the impact of α/α_{ref} in Fig. 6(a). Buoyancy-driven convection and diffusion act as the regenerating processes, hence t_{relax} is plotted over β/β_{ref}, $D^{(1)}/D^{(1)}_{ref}$ in Fig. 6(b,c).

By contrast, the moderate variation of r only has a minor influence on the characteristic oscillation times of our system (less than 5 s on t_{relax} and less than 1 s on t_{rise}) and therefore is not shown in a separate graph. The same applies to the dependence of t_{relax} on α and t_{rise} on β, $D^{(1)}$ which is equally weak. For large α, representing a strong surfactant, the high Marangoni velocities in the active phase are able to mix the surrounding fluid in a very short time. The velocity profiles in Fig. 5(b) show that the interfacial convection directed downwards largely exceeds the upstream supported by buoyancy convection at a larger distance from the droplet surface. Diffusion of solute is an even slower process, hence the value of alpha dominates t_{rise}.

Due to the reduced interfacial convection in the relaxation phase, β and $D^{(1)}$ become effective. Large β means that the upstream in the surrounding liquid is augmented so that the mixed, solute-rich fluid quickly returns to the upper regions what significantly shortens the duration of t_{relax} in Fig. 6(b). However, the progression of t_{relax} in Fig. 6(c) emphasizes that diffusion is necessary to sufficiently redistribute the mixing zone. The diffusive time scale for the reference simulation can be estimated as $\tau_{diff} = (2r)^2/D^{(1)}_{ref}$ where the droplet diameter $2r$ is used as a characteristic length scale. The obtained value $\tau_{diff} = 83$ s agrees in its order of magnitude with the observed relaxation time. Slowly diffusing solutes like long-chain molecules result in extremely long relaxation times while the oscillations are high-frequent for large $D^{(1)}$. This trend is also relevant for the thermocapillary case since thermal diffusivities considerably exceed solutal values. Furthermore, the curves for α/α_{ref}, β/β_{ref} confirm the experimentally

observed frequency dependence on the concentration gradient. A higher concentration gradient yields both higher gradients in interfacial tension and solution density. Both effects result in a higher oscillation frequency, but Fig. 6 indicates that the larger contribution to this is coming from β.

3.2 Multidroplet configurations

3.2.1 Droplet interaction in experiment

In the experimental results of Sec. 3.1.1, the temporal evolution of the relaxation oscillations at droplet 4 (cf. Fig. 2) was excluded. As already noted in this Section, the approximation based on pure diffusion is not able to fully capture the actual concentration distribution around the droplets due to the additional convective mass transfer. The Marangoni flow at the surface of the droplets locally pushes the concentration front further into the aqueous bulk phase. This effect can even induce relaxation oscillations at neighboring droplets. Fig. 7 illustrates such an interaction between droplet 3 and 4. Droplet 3 is subjected to a higher concentration gradient because of its smaller distance to the interface of the two-layer system. Fig. 7(a), upper image, shows a phase of active Marangoni convection at droplet 3. Its mixing zone grows and conveys fluid rich in 2-propanol to the lower regions. In this way, Marangoni convection is initiated at droplet 4, see Fig. 7(a), lower image. The Marangoni vortex at droplet 4 takes on the solute-rich fluid built up around droplet 3 and thereby is amplified. When the concentration gradient in the surrounding of both droplets is erased, the active phase again expires. By this interaction, droplet 3 transfers its oscillation frequency to droplet 4. The temporal evolution of convection in Fig. 7(b) almost matches except a slight leading of droplet 3 (corresponding to a marginal phase difference) due to the start-up of convection. Such a mode-locking of temporal or spatial periodicity, where a certain frequency is imposed by coupling effects, is a known phenomenon in nonlinear systems[55]. We now employ this coupling to propagate a signal in a multidroplet configuration.
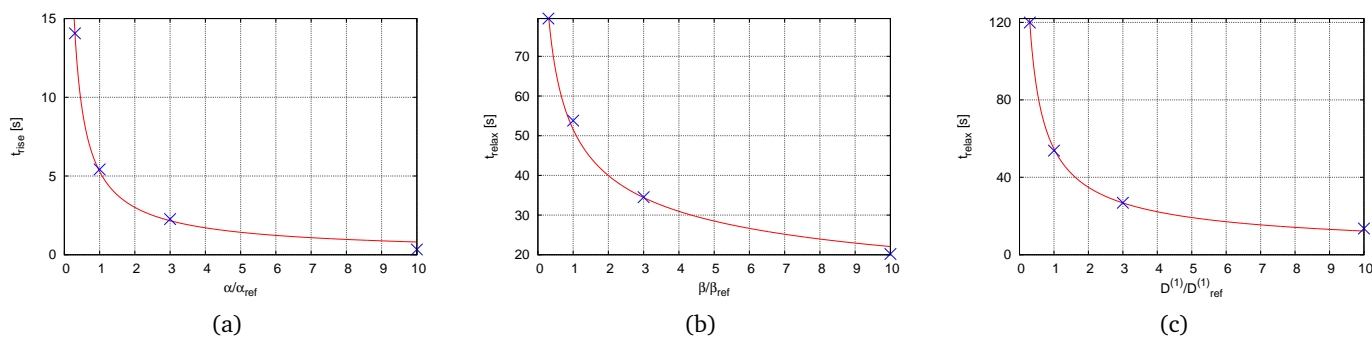
Fig. 6 Time span of increasing (a) and decreasing (b,c) surfactant concentration for varied values of α and β, $D^{(1)}$ relative to the reference simulation.
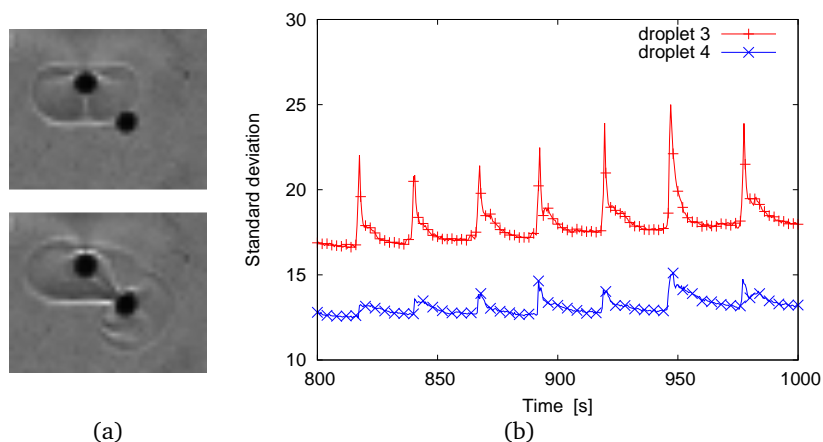

Fig. 7 Interaction of Marangoni convection between droplet 3 and 4: (a) shadowgraph images showing the structure of the flow, (b) standard deviation of gray value distribution around each droplet showing the strong coupling of oscillation frequency. The position of these droplets in the two-layer system is depicted in Fig. 2(a).

3.2.2 Droplet interaction in simulation

3.2.2.1 Two droplets. In this section, we perform a numerical distance study of pairwise droplet interaction which then serves as a basis to arrange ensembles of multiple droplets. The surface-to-surface distance is varied from 0 mm to 3 mm (i.e. up to tenfold droplet diameter). Note that the limiting case of touching spheres primarily is of theoretical interest since coalescence has to be considered for this configuration. Three different distances in this range are shown in Fig. 8(a) to 8(c). The position of the upper droplet remains fixed. The vertical position (y-coordinate) of the lower droplet is changed in every simulation, whereas its horizontal position (x-coordinate) is held constant. From the evolution of the mean interface concentration, e.g. Fig. 8(d), the dominant oscillation frequency is extracted using fast Fourier transformation. This evaluation is performed in the time interval $t \in [200\,s, 800\,s]$ to ensure that the system is settled after the initial oscillations with higher amplitudes and slightly different period lengths. Thereby, the dominant frequencies in the later stages are captured. Furthermore, an interval length of $600\,s$ is sufficient to capture enough periods for every case of the droplet distances.

Three ranges (A, B, C) with different behavior can be distinguished when the dominant frequency of the upper (red curve, plus symbols) and the lower droplet (blue curve, crosses) is plotted over the distance in Fig. 9. At small distances (interval $[0, 1.3\,mm]$, range A), the oscillation frequency of both droplets perfectly matches due to the direct coupling as already observed in the experiment. Fig. 8(d) shows an example of the transition region B which is detailed below. In range C, i.e. for distances larger than approx. 1.9 mm, the droplet oscillations become rather independent in Fig. 9. In the theoretical case of infinite droplet distance, the oscillation frequency should be equal for the upper and lower droplet, i.e. the blue and red curve should again coincide. However, the dominant frequencies of the lower droplet vary around the value for the upper droplet in range C. Those variations probably are caused by following effects: Firstly, in our phase field model, the initial grid is locally refined near the interface. Depending on the droplet position, the mesh around the droplet interface may change marginally due to this adaptation which leads to slightly different concentration gradients along the interface. Secondly, the upper droplet causes mixing of the solute inside the Hele-Shaw cell. Even if the mixing is not strong enough to create a noticeable frequency coupling at such a large distance, it still changes the concentration gradients in the region above the lower droplet influencing its oscillation frequency.

Range B corresponds to intermediate droplet distances lying in
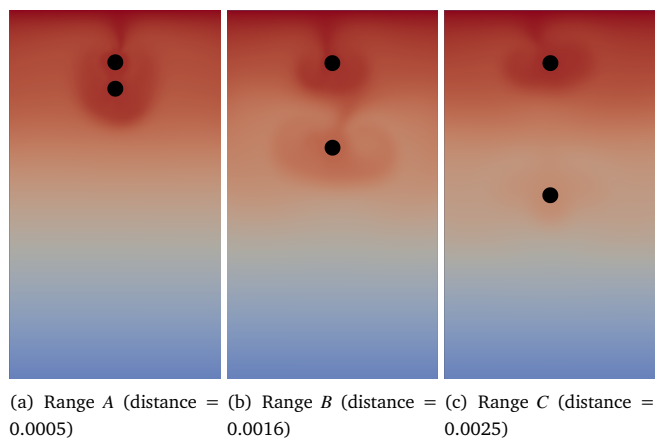
(a) Range A (distance = 0.0005)

(b) Range B (distance = 0.0016)

(c) Range C (distance = 0.0025)
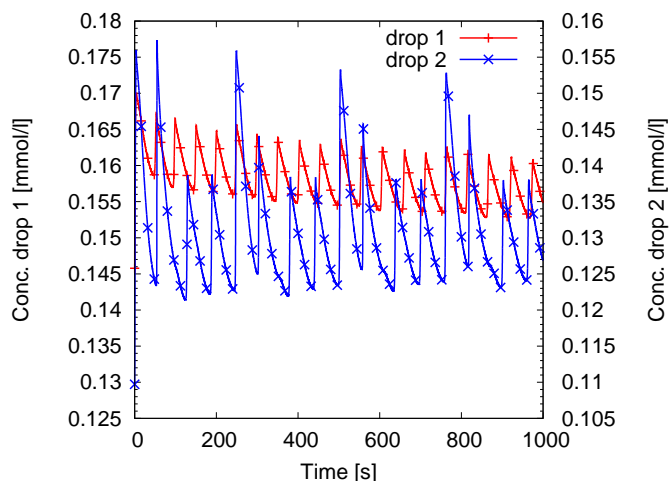
(d) Mean solute concentration over time of two droplets in range B with a distance of 1.2 mm. Seperate y-axes are used for both droplets to enhance comparability of periodic behaviour of the two droplets.

Fig. 8 (a) - (c): Examples of the droplet positions for the three ranges observed in Fig. 9. A section of 4 mm × 7 mm of the whole domain size of 8 mm × 10 mm is shown. (d) Solute concentration over time for one example case in range B.

the interval $[1.3, 1.9\,\text{mm}]$. Here, the distances are too large for an instantaneous coupling and too small for quasi independent oscillations. This leads to strong variations in the dominant frequencies in range B since the partial influence of the upper droplet may cause less periodic and more irregular behavior of the lower droplet. Fig. 8(d) illustrates the oscillations of the mean solute concentration over time for an example distance of 1.2 mm. For the upper droplet, the periodicity of the process remains regular and similar to other distances. The oscillations of the lower droplet vary in amplitude and frequency. One observes a periodicity every four pulses (e.g. $t \in [250\,\text{s}, 500\,\text{s}]$). Within those larger periods, the first two pulses feature high amplitudes and are synchronized with the pulses of the upper droplet. The remaining two pulses have lower amplitudes and are not synchronized with the upper droplet. At other distances in range B, also temporary synchronization was observed, i.e. a frequency locking of both droplets over a limited time span. Furthermore, different integer frequency ratios (e.g. 1:4) occurred due to the partly coupled oscillations of both droplets. The partial synchronization is no longer noticeable at the larger distances in region C. A detailed analysis of the complex behavior in range B is beyond the scope of the present work. Fig. 9 rather is used to determine suitable droplet distances for our investigations with multidroplet ensembles. Therefore, we choose a value within range A to ensure direct transmission of the stimulation from one droplet to the next.

3.2.2.2 Droplet chains. For the multidroplet simulations, we choose two chain configurations displayed in Fig. 10 and Fig. 11 as basic examples for information transmission along different paths. Twelve 0.3 mm-sized droplets are arranged in a linear droplet chain and in a quarter-circular arc with the same x, y-position of the first droplet and with a distance of 0.5 mm in the linear case and 0.44 mm in the quarter-circular case.

Indeed, the relaxation oscillations now are initiated over the whole droplet ensemble as shown in Fig. 12 by the progression
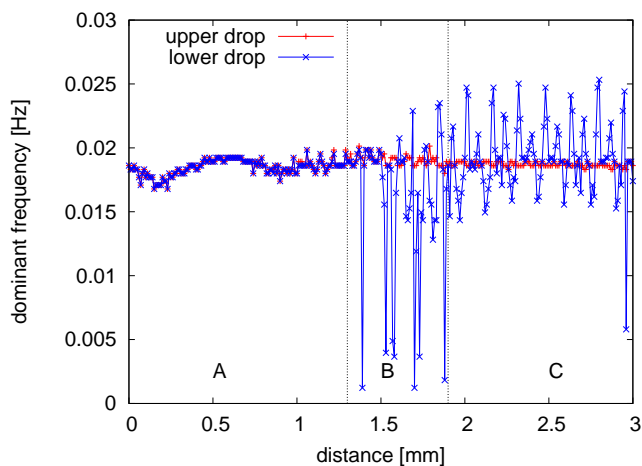

Fig. 9 Dominant frequencies of two vertically aligned droplets with different distances. The position of the lower droplet is changed in y-direction only, whereas the position of the upper droplet remains unchanged. Dotted vertical lines distinguish between range A, B, and C (described in the text), respectively. Note that these lines are only for illustration, as there is a smooth transition between the ranges.

of the mean solute concentration at the upper (red curve, plus symbols) and the lowest droplet (blue curve, crosses). Fig. 10 and Fig. 11 depict different stages of one ensemble oscillation cycle. Starting from an adjacent concentration distribution similar to the bulk, the active phase of Marangoni convection sets in at the first droplet in Fig. 10(a) since it is located nearest to the upper boundary with fixed concentration. Subsequently (b), a front of high solute concentration (regions of increasingly red color) is transported downwards to the last droplet. At the end of the active phase (c), a jet of solute-rich fluid has even penetrated the bulk below the last droplet. This low-density fluid first rises at the side of the droplet chain. However, after termination of the Marangoni-driven downstream (d), an ascending solute front

develops, now passing the droplets in reverse direction. For the circular arc in Fig. 11, the downstream of solute-rich fluid proceeds similar to the linear case. However, the lower droplets are positioned nearly horizontally. This reduces the overall concentration gradient acting at the droplet ensemble so that the penetration depth of the solutal jet is smaller. Furthermore, it leads to different characteristics in the relaxation phase. The mushroom-shaped buoyant plume rises directly above the last droplets, i.e. passing the ensemble sideways without pronounced interaction. Videos V1 and V2 in the supplementary material further illustrate the whole process.

Next, we examine how these differences impact the oscillations of the mean solute concentration in the linear case (subscript l) and the circular arc (subscript c) in Fig. 12. In Fig. 12(a) around $t = 160\,$s, one observes a concentration increase during the active phase of $\Delta c_{1,l} = 3.409 \cdot 10^{-5}\,$mol/l at the first droplet and $\Delta c_{12,l} = 1.131 \cdot 10^{-5}\,$mol/l at the last droplet. For the circular arc in Fig. 12(b), the oscillation amplitudes at the first ($\Delta c_{1,c} = 3.421 \cdot 10^{-5}\,$mol/l) and at the last droplet ($\Delta c_{12,c} = 1.095 \cdot 10^{-5}\,$mol/l) are almost identical to linear case. With regard to the oscillation frequency, a more pronounced influence of the droplet configuration is obtained. Due to the larger overall concentration gradient, we observe smaller oscillation periods of 39.7 s in the linear case and longer periods of 59.7 s for the circular arc. The interaction with the buoyant rise for the linear chain causes additional sub-pulses (see secondary peaks at blue curve in Fig. 12(a)) which are absent for the circular arc.

To quantify the rate of information transmission, we define a velocity v

$$v = \frac{l}{\Delta t}, \tag{4}$$

where l is the (arc) length of the droplet chain and Δt is the length of time between the peaks of mean solute concentration at the first (upper) and last (lowest) droplet, resulting from the phase difference of the oscillations. In Fig. 13, v is plotted over time. The data points are drawn at the time when the peak at the first droplet is reached. Besides the droplet chains in linear and circular arc configuration, we include the simulation with two droplets and the same droplet-to-droplet distance for comparison. At small times, a considerable velocity decrease can be observed in Fig. 13 for all configurations since the initial linear concentration gradient induces a strong mixing which changes the concentration distribution for the subsequent oscillations. The droplet pair soon tends to a constant, but relatively low velocity. For the linear droplet chain, the highest velocity values are obtained because the acting concentration difference along the characteristic (vertical) length of the whole ensemble, i.e. the Marangoni driving force is significantly larger. Furthermore, the large characteristic length leads to an increase of the restoring force by buoyancy convection. Hence, the velocity curve stays on a higher level throughout the whole simulation time. The variance of the curve progression for the linear case is due to the above-mentioned sub-pulses, which influence the specific time for the first local maximum of one oscillation period at the last droplet. As can be seen in Fig. 12(a) (e.g. around $t = 250\,$s), the sub-pulses become more pronounced in the later stage.

The ensemble effects are reduced at the circular arc. Firstly, the vertical length of the circular ensemble which is relevant for the acting concentration gradient is smaller by a factor of 0.58 compared to the linear chain. Secondly, the nearly horizontally arranged last droplets have a retarding effect since the initial concentration gradient along the lower end of the circular arc tends to zero. Nevertheless, in the observed time span, the transfer rate for this ensemble configuration still exceeds the droplet pair.

4 Summary and outlook

To demonstrate the versatility of the system, the first part of our study investigates the characteristics of solutal Marangoni-driven relaxation oscillations at single droplets. The signal dynamics generated by this effect can be tuned via the material parameters of the employed substances. Based on the experimentally observed feedback between the oscillations at neighboring droplets, the simulations use this phenomenon to propagate a signal along a defined path in multidroplet configurations. The ensemble effects enhance the transfer characteristics, as the solute transport velocity in a vertical droplet chain considerably exceeds the two-droplet case. It even is possible to bridge over a blind area of horizontally arranged droplets where concentration gradients initially are absent.

The various coupling modes and the transient synchronization observed in our simulations with intermediate droplet-to-droplet distances provide interesting phenomena for subsequent research. However, our study is not only an intriguing example of spatio-temporal structure formation due to ensemble interactions in oscillator networks. It specifically addresses information transmission at length scales relevant for microfluidic applications. Since the local concentration gradients may be inherent in the process, e.g. in consequence of surfactant consumption or production in a chemical reaction, the oscillatory flow can directly reveal information about the process state. To adapt our model configuration to microfluidic geometries, the influence of near system boundaries on the coupling of the droplets has to be investigated. Furthermore, future work is necessary to create well-defined droplet (or bubble) alignments for first microfluidic experiments. A promising approach is the droplet attachment at hydrophobic spots on the solid substrate[4]. Tools to produce such substrate structures in microfluidic devices, also suitable for mass manufacturing, are already available[56]. Preliminary simulations on diverse configurations shown in Fig. 14 such as looping, splitting or merging droplet chains underline the geometrical flexibility which could be reached by a combination with substrate patterning techniques.

Acknowledgements

(a) start-up of active phase   (b) front propagation   (c) end of active phase   (d) relaxation phase
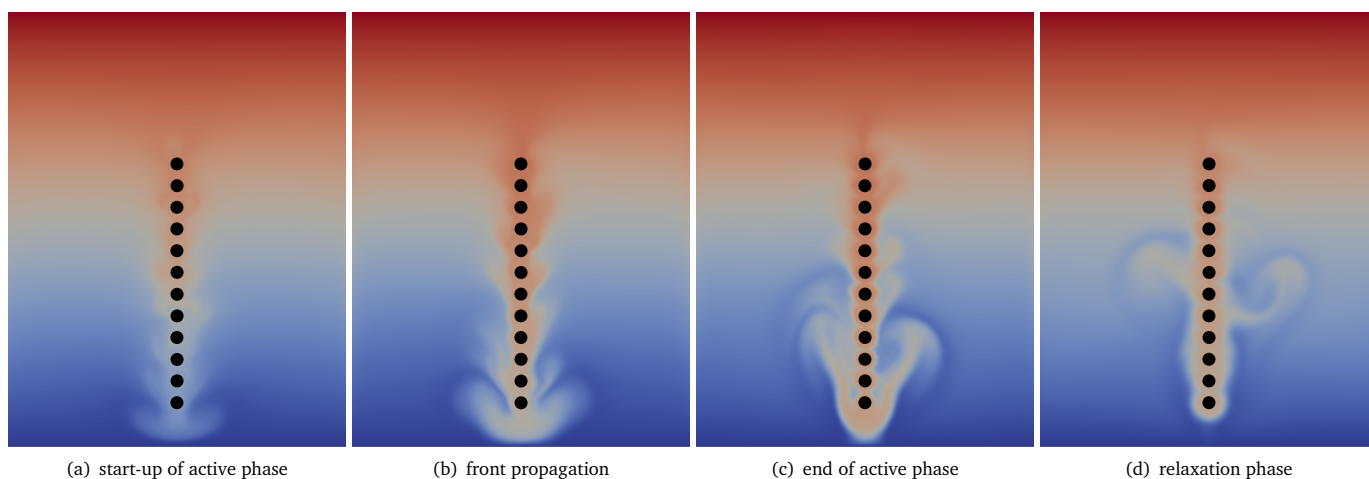
Fig. 10 Snapshots of one oscillation cycle for the linear droplet chain.

(a) start-up of active phase   (b) front propagation   (c) end of active phase
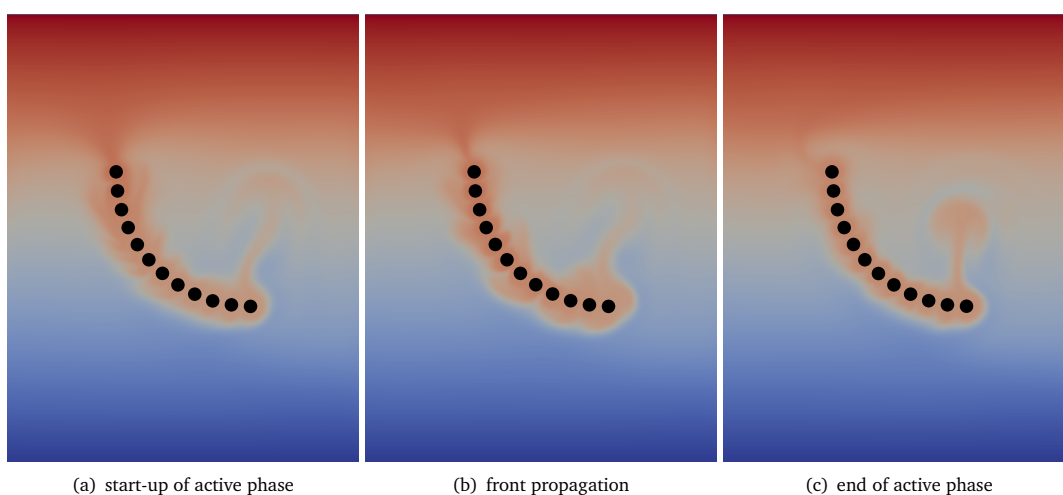
Fig. 11 Snapshots of one oscillation cycle for the droplets arranged in a quarter-circular arc.
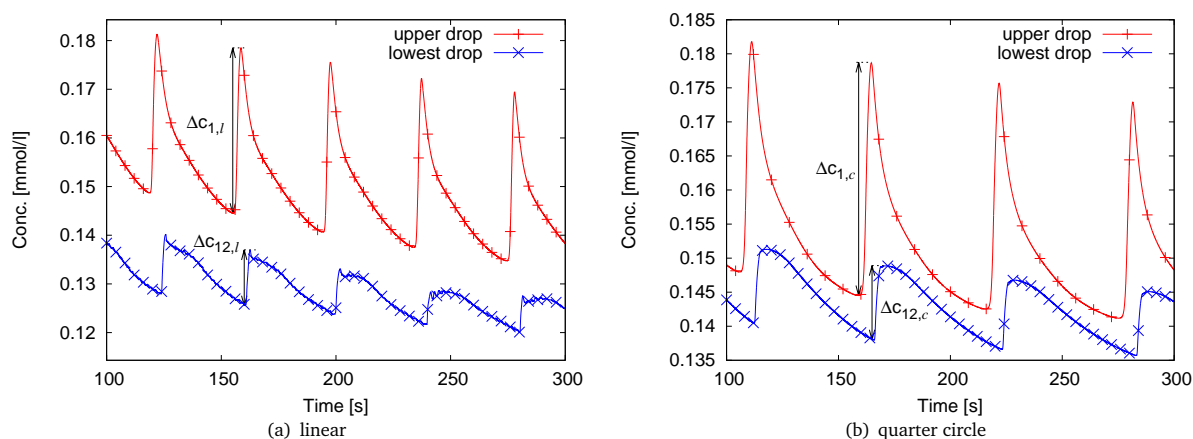

(a) linear   (b) quarter circle

Fig. 12 Mean solute concentration over time for (a) linear and (b) circular arc droplet chain configurations. Upper curves refer to the first, lower curves to the last droplet of the chain.

References

1 E. De Leo, L. Galluccio, A. Lombardo and G. Morabito, *Nano Communication Networks*, 2012, **3**, 217–228.

2 N. Farsad, H. B. Yilmaz, A. Eckford, C.-B. Chae and W. Guo, *IEEE Communications Surveys & Tutorials*, 2016, **18**, 1887–
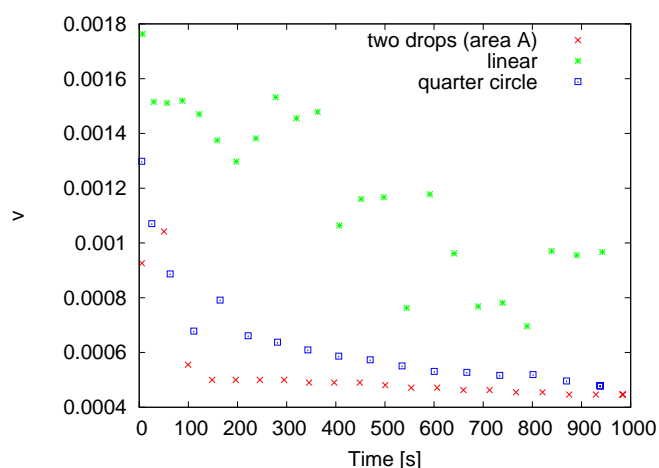
Fig. 13 Signal transport velocity $v = l/\Delta t$ characterizing the transmission speed of the oscillations over time for three multidroplet configurations.

1919.

3 J. Ju and J. Warrick, *Biochip Journal*, 2013, **7**, 361–366.

4 D. K. Sinz, M. Hanyak and A. A. Darhuber, *The Journal of Physical Chemistry Letters*, 2013, **4**, 1039–1043.

5 T. Yamada and N. Ono, *Journal of Micro and Nano-Manufacturing*, 2015, **3**, 021003.

6 A. A. Darhuber and S. M. Troian, *Annu. Rev. Fluid Mech.*, 2005, **37**, 425–455.

7 M. Sellier, V. Nock and C. Verdier, *International Journal of Multiphase Flow*, 2011, **37**, 462–468.

8 V.-V. Ng, M. Sellier and V. Nock, *Acta Mechanica*, 2018, **229**, 571–584.

9 A. S. Basu and Y. B. Gianchandani, *Journal of Micromechanics and Microengineering*, 2008, **18**, 115031.

10 T. A. Arshad, C. B. Kim, N. A. Prisco, J. M. Katzenstein, D. W. Janes, R. T. Bonnecaze and C. J. Ellison, *Soft Matter*, 2014, **10**, 8043–8050.

11 J. P. Singer, *Journal of Polymer Science Part B: Polymer Physics*, 2017, **55**, 1649–1668.

12 V. X. Nguyen and K. J. Stebe, *Physical Review Letters*, 2002, **88**, 164501.

13 X. Yang, C. Y. Li and Y. Sun, *Soft Matter*, 2014, **10**, 4458–4463.

14 K. Schwarzenberger, T. Köllner, H. Linde, T. Boeck, S. Odenbach and K. Eckert, *Advances in Colloid and Interface Science*, 2014, **206**, 344 – 371.

15 S. G. Yiantsios, S. K. Serpetsi, F. Doumenc and B. Guerrier, *International Journal of Heat and Mass Transfer*, 2015, **89**, 1083–1094.

16 T. Köllner, K. Schwarzenberger, K. Eckert and T. Boeck, *Journal of Fluid Mechanics*, 2016, **791**, R4.

17 J. R. Picardo, T. Radhakrishna and S. Pushpavanam, *Journal of Fluid Mechanics*, 2016, **793**, 280–315.

18 S. Shin, I. Jacobi and H. A. Stone, *Europhysics Letters*, 2016, **113**, 24002.

19 F. Wodlei, J. Sebilleau, J. Magnaudet and V. Pimienta, *Nature communications*, 2018, **9**, 820.

20 M. Lappa, *Physics of Fluids*, 2006, **18**, 042105.

21 J. Grawitter and H. Stark, *Soft Matter*, 2018, **14**, 1856–1869.

22 S. Thutupalli, R. Seemann and S. Herminghaus, *New Journal of Physics*, 2011, **13**, 073021.

23 S. Herminghaus, C. C. Maass, C. Krüger, S. Thutupalli, L. Goehring and C. Bahr, *Soft Matter*, 2014, **10**, 7008–7022.

24 S. Tanaka, S. Nakata and T. Kano, *Journal of the Physical Society of Japan*, 2017, **86**, 101004.

25 Y.-J. Chen, K. Sadakane, H. Sakuta, C. Yao and K. Yoshikawa, *Langmuir*, 2017, **33**, 12362–12368.

26 D. L. Koch and G. Subramanian, *Annual Review of Fluid Mechanics*, 2011, **43**, 637–659.

27 M. J. B. Hauser and L. Schimansky-Geier, *The European Physical Journal Special Topics*, 2015, **224**, 1147–1150.

28 I. H. Riedel, K. Kruse and J. Howard, *Science*, 2005, **309**, 300–303.

29 M. Fauvart, P. Phillips, D. Bachaspatimayum, N. Verstraeten, J. Fransaer, J. Michiels and J. Vermant, *Soft Matter*, 2012, **8**, 70–76.

30 S. Basu, Y. Gerchman, C. H. Collins, F. H. Arnold and R. Weiss, *Nature*, 2005, **434**, 1130.

31 C. Kirst, M. Timme and D. Battaglia, *Nature communications*, 2016, **7**, 11061.

32 G. Gerisch, D. Hülser, D. Malchow and U. Wick, *Phil. Trans. R. Soc. Lond. B*, 1975, **272**, 181–192.

33 J. Selimkhanov, B. Taylor, J. Yao, A. Pilko, J. Albeck, A. Hoffmann, L. Tsimring and R. Wollman, *Science*, 2014, **346**, 1370–1373.

34 O. Steinbock, A. Lange and I. Rehberg, *Phys. Rev. Lett.*, 1998, **81**, 798–801.

35 J.-M. Ginoux and C. Letellier, *Chaos: An Interdisciplinary Journal of Nonlinear Science*, 2012, **22**, 023120.

36 H. Jehring, N. V. Huyen and E. Horn, *Journal of Electroanalytical Chemistry and Interfacial Electrochemistry*, 1978, **88**, 265–268.

37 A. Zuev and K. Kostarev, *Journal of Experimental and Theoretical Physics*, 2006, **103**, 317–323.

38 R. Birikh, A. Zuev, K. Kostarev and R. Rudakov, *Fluid Dynamics*, 2006, **41**, 514–520.

39 K. Kostarev, A. Shmyrov, A. Zuev and A. Viviani, *Experiments in Fluids*, 2011, **51**, 457–470.

40 K. Schwarzenberger, S. Aland, H. Domnick, S. Odenbach and K. Eckert, *Colloids and Surfaces A*, 2015, **481**, 633–643.

41 N. Kovalchuk and D. Vollhardt, *Advances in Colloid and Interface Science*, 2006, **120**, 1 – 31.

42 N. Kovalchuk and D. Vollhardt, *Colloids and Surfaces A: Physicochemical and Engineering Aspects*, 2006, **291**, 101–109.

43 N. Kovalchuk and D. Vollhardt, *The Journal of Physical Chemistry B*, 2005, **109**, 15037–15047.

44 A. Mizev and R. Birikh, *The European Physical Journal Special Topics*, 2011, **192**, 145–153.

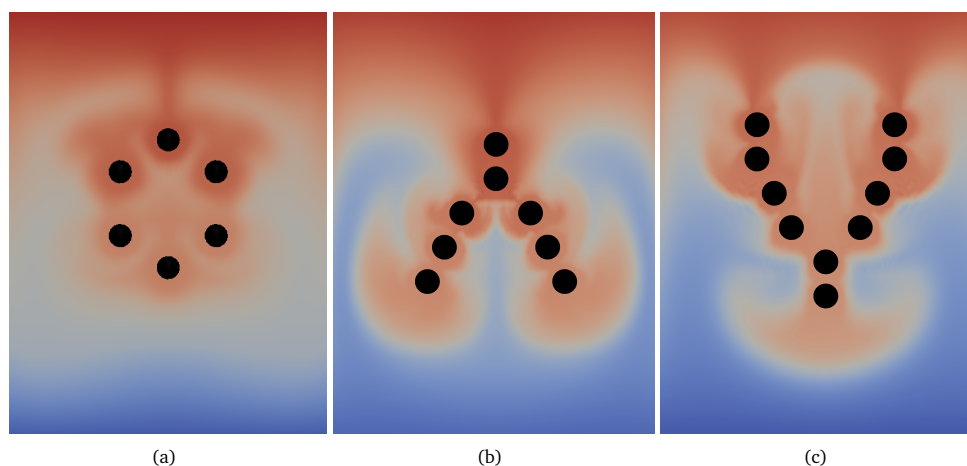45 Y. Shi and K. Eckert, *Chemical Engineering Science*, 2008, **63**, 3560–3563.

Fig. 14 Example configurations of looping (a), splitting (b), and merging (c) droplet chains.

46 D. Lide, *CRC Handbook of Chemistry and Physics: A Ready-Reference Book of Chemical and Physical Data*, CRC Press, Boca Raton, FL, 2004.

47 Carl Roth GmbH & Co. KG, *Specification of paraffin oil, Ph.Eur., DAB, low viscosity*, 2014.

48 G. W. Paul and L. E. M. De Chazal, *Journal of Chemical & Engineering Data*, 1967, **12**, 105–107.

49 W. Hayduk and H. Laudie, *AIChE Journal*, 1974, **20**, 611–615.

50 J. Li and P. W. Carr, *Analytical Chemistry*, 1997, **69**, 2530–2536.

51 K. E. Teigen, P. Song, J. Lowengrub and A. Voigt, *Journal of computational physics*, 2011, **230**, 375–393.

52 W. Boos and A. Thess, *Journal of Fluid Mechanics*, 1997, **352**, 305–330.

53 W. Merzkirch, *Flow visualization*, Academic Press, London, 1987.

54 J. Crank, *The Mathematics of Diffusion*, Clarendon Press, Oxford, 1975.

55 H. Haucke and R. Ecke, *Physica D: Nonlinear Phenomena*, 1987, **25**, 307 – 329.

56 M. S. A. Ali Kemal Yetisen and C. R. Lowe, *Lab on a Chip*, 2013, **13**, 2210–2251.